Biomass Self-Nitrogen Doped Mesoporous Carbon Electrode for Supercapacitors

Chika A. Okonkwo[1], Obioma E. Achugbu[2], Ifeoma ObioraOkafor[2], Ukamaka V. Alison[3]

[1]Directorate of Research and Innovation, Nnamdi Azikiwe University Awka Nigeria

[2]Chemical Engineering Department, Nnamdi Azikiwe University Awka Nigeria

[3]Computer Science Education Department, Nnamdi Azikiwe University Awka Nigeria

DOI: https://doi.org/10.51584/IJRIAS.2024.908025

Received: 08 July 2024; Revised: 31 July 2024; Accepted: 03 August 2024; Published: 05 September 2024

ABSTRACT

Doping and surface modification of porous carbon materials derived from biomass are part of the research hotspots that promote high performance and low cost of electrode materials for supercapacitors, owing to advantage of tunable unique structure of renewable biomass. Nitrogen-rich spirulina extract impregnated castor shell was used to effectively regulate and modify the surface morphology of biomass carbon by KOH activation and high-temperature calcination. The prepared porous carbon exhibits nitrogen-rich micro-mesoporous carbon with unique interconnected network structure and higher specific surface area (1527 m^2g^{-1}) after the high temperature treatment for supercapacitor electrode. The nitrogen-rich organic functional groups derived from extract of spirulina improve interaction of KOH and castor shells responsible for formation of unique interconnected micro-mesoporous structure. The as-prepared nitrogen doped micro-mesoporous carbon contributes to enhance charge transfer, and to decrease mass transfer resistance of supercapacitor electrode. A good electrochemical performance with high specific capacitance of 333 F g^{-1} at 1 A g^{-1} was obtained. The charge/discharge cycling behavior shows only loss of 0.3 % of total capacity after 10,000 cycles at 10 A g^{-1}. The two-electrode configuration of assembled CSSK material displayed a remarkable energy density of 10 Wh kg^{-1} at a power density of 600 W kg^{-1} and good cycling behavior (after 10000 cycles 91.7 % retention of specific capacitance). Thus, strategy of the extract mediated synthesis is facile and effective to improve the performance of porous carbon for promising candidates as low-cost electrode materials for supercapacitors.

Keywords: Biomass, Nitrogen, Doped, Carbon, Supercapacitor

INTRODUCTION

Supercapacitors are widely used in consumer electronics, electric vehicles, and pulsing technology among others that required durability, and so special need for high performance electrode material. Particularly, porous carbons excel in study as the main electrode material, owing to excellent property, including unique large specific surface and chemical stability which essentially improves the performance at relatively low cost for supercapacitor[1,2]. Biomass as a precursor for new environmentally friendly carbon materials is converted into various porous carbon materials as electrode for high performance in charge and discharge processes of EDLCs[3, 4]. However, the biomass carbonization is a complex process which contains many chemical reactions such as dehydration, decomposition, condensation and polymerization etc.[5] Introduction of an activation reagent such as KOH[6], $CaCO_3$[7], H_3PO_4[8] etc. in the carbonization process to obtain special structure of the porous carbon electrode material has been a promising technology. Especially the rich micro-mesoporous structure carbon shows good performance for supercapacitors, which is attributed to large specific surface area and excellent charge transmission channel in efficient electrodes[9,10]. Heteroatoms doping (nitrogen and oxygen etc.) can uniquely improve the performance of carbon electrodes by inducing pseudo-charge transmission channel[11,12]. Therefore searching for biomass as precursor and synthesis mothed of porous carbons has been

very useful for advancing the supercapacitor performance[13-15]. Sun et al.[16] synthesized biomass-derived nitrogen-doped micro-mesoporous carbons with high specific surface area from silkworm cocoon for electrode. However, the carbonization activation process of lignin and cellulose based natural plants biomass is conventionally complicated and difficult to form promising porous carbon structure. Furthermore, the limited nitrogen content of conventional lignin and cellulose based biomass not conducive to synthesize high performance nitrogen doped carbon materials.

Recently, Gao et al.[17] prepared micro-mesoporous carbon from algae (Enteromorpha prolifera) by a self-template method. Algae contain carboxylic/hydroxyl groups and mineral salts as a precursor induced a special porous carbon structure to enhance the performance of the electrode materials[18-20]. The composition of algae mainly includes proteins, polysaccharides and lipids etc. Especially, spirulina are easily liquefied into water-soluble organic matter rich in nitrogen functional groups which similar to soluble organic reagents for nitrogen doping as nitrogen sources[20, 21]. Inspired by these studies, we attempted to design the extract of spirulina induce the carbonization of natural nutshell biomass to form specific micro-mesoporous structure.

In this work, the novel nitrogen-rich extract of spirulina to impregnate castor shell powder derived from castor processing waste for forming infiltrated networks as precursor with KOH to synthesize nitrogen doped micro-mesoporous carbon was investigated. The organic groups of the spirulina extract improve the interaction between KOH and castor shells to induce the formation of unique interconnected networks micro-mesoporous structure with higher specific surface area by high temperature activation process was investigated. The as-prepared nitrogen-rich micro-mesoporous carbon materials for electrode are studied to improve performance of supercapacitor. The use of microalgae extract indeed contributes to improve the structure and surface properties of porous carbons derived from biomass by more effective carbonization/activation and it is a renewable green synthetic route for micro-mesoporous carbon electrode materials.

Experiment Section

Syntheses of Spirulina Extract

The purchased *spirulina* powder (Forrida bio-health technology Co. LTD, Beijing, China), without further treatments, was characterized by FTIR and elemental analysis, and results are shown in **Figure 5** and **Table 1**. The amounts used for hydrothermal process, 2 grams of *spirulina* powder, were well dispersed in 50 mL deionized water at room temperature. The completed heating process in autoclave for 4 h at 200 degree was gradually cooled to room temperature, and extract concentration of 37.5 g L^{-1} was obtained by filtration and centrifugation and called water soluble *spirulina* extract (SE). As a nitrogen dopant, it contains 9.53 % nitrogen (see table2).

Castor shell powder (CSP) from Shandong Zibo Jiaxiang Castor Seed Industry Technology Co., Ltd, China, with ground particles less than 200 mesh in 2 grams, was impregnated in 4 mL of the *Spirulina* extract at 40 ℃ overnight. Subsequently, the functionally bonded extract/CSP was made paste with 2 mL of KOH (2 M) activator, allowing intercalation of potassium ions into the coated structure for effective activation at 40 ℃ overnight. The functional interactivity equilibrium was reached by drying the paste at 80 ℃ for 24 h. Then, decomposition reaction was performed, using calcination temperature of 800 ℃, and the process was controlled under nitrogen atmosphere gas for 4 hours, also cooled down gradually to room temperature. All the traces of inorganic salt were removed with 2 M hydrochloric acid, and the dried sample designated CSSK was characterized structurally. Investigated contributions of the *spirulina* extract and KOH activator were completed by elimination method to synthesize comparable samples designated CSS without KOH activator and CSK without *spirulina* extract. The process of the syntheses are maintained like that of CSSK, and the sample without extract and activator is designated CSC.

Characterization

Powder X-ray diffraction (XRD) was recorded on an X'Pert Pro X-ray diffractometer (PANalytical BV, Netherlands) with Cu Kα radiation at a voltage of 40 kV and a current of 30 mA. The morphology and structure of the samples were further analyzed by using LEO 1530 Scanning Electron microscope (SEM) and

ISSN No. 2454-6194 | DOI: 10.51584/IJRIAS |Volume IX Issue VIII August 2024

Philip Analytical FEI Tecnai 30 high resolution transmission electron microscope (TEM) at an accelerating voltage of 300 kV. The Brunauer-Emmett-Teller (BET) specific surface area, pore volume and pore size distribution were measured by ASAP 3020 Micromeritics instrument. Fourier transform infrared spectroscopy (FTIR) was performed on a FTIR Nicolet Avatar 330 (Nicolet, USA) instrument. The spectra were recorded in the region of 4000-400 cm^{-1} using condition of 32 scans at a 2 cm^{-1} resolution. Raman spectroscopy was acquired using a HORIBA Xplo RA Raman spectrometer with a laser excitation wavelength of 532 nm and a power of 16 mW. X-ray photoelectron spectroscopy (XPS) was carried out using a Qtac-100 LEISS-XPS instrument with a monochromatized micro focused Al X-ray source. The binding energy was calibrated by C 1s peak at 284.8 eV. Organic elemental analysis was carried out using an Elementar analyzer (varioEL III Elementar).

Electrochemical Measurements

The electrochemical measurements were measured by cyclic voltammetry (CV), chronopotentiometry (CP), and A.C. impedance techniques, using a computer-controlled potentiostat: CHI660D electrochemical workstation at ambient temperature. The composition of the electrodes is the same for three-electrode and two-electrode test systems. The working electrode was prepared by mixing the asprepared materials, acetylene black, and polytetrafluoroethylene (PTFE) in a mass ratio of 8:1:1, the mixture was rolled into films of uniform thickness (~0.1 mm) and followed by drying at 60°C for 12 h. Finally, the films were pressed into nickel foam current collectors with a tablet press. Three different electrodes were formed with the activated CSK, CSS and CSSK. They were wetted in electrolyte to equilibrium of electrolyte ions on the carbon electrode surface, and the maximum wetting time is 1.5 h with 10 times rerun scan at rate of 5 mV s^{-1}. Standard 6 M KOH electrolytic solutions were used for both systems.

In three-electrode system comprising counter, working, and reference (Hg/HgO tube) electrodes, the current density was obtained within potential window of -0.5 to 0.2 V at various scan rates: 20, 40, 60, 80, and 100 mV s^{-1}. Galvanostatic charge-discharge (GCD) process was completed with usable potential range from -0.5 to 0.2 V versus time. Electrochemical impedance (EIS) of the electrodes was measured, the frequency range is 0.01 Hz to 10 kHz, and the alternating voltage amplitude is 5 mV. Parameters of capacitance for two-electrode and three-electrode systems are stated in equation (5-1), respectively. Energy and power densities were calculated using equation (2) and (3), respectively.

$$\mathbf{Cg = (I * \Delta t)/ (m * \Delta V)} \qquad \textbf{Equation 1}$$

Where C_g (F g^{-1}) is the gravimetric capacitance, I (A) is the discharge current, m (g) is the mass of active electrode, Δt (s) is the discharge time, and ΔV (V) is the potential window.

Specific energy density (E) is calculated as following; in a unit of watt-hour per kilogram (Wh kg^{-1}):

$$\mathbf{E = (1/ (2*3.6))\ C_g\ V^2} \qquad \textbf{Equation 2}$$

Where, E (Wh Kg^{-1}) is the specific energy density, V^2 (V) is the operating voltage calculated from $V_{max} - V_{min}$ at IR drop.

$$\mathbf{P = E/\Delta t*3600} \qquad \textbf{Equation 3}$$

P (W Kg^{-1}) is the specific power density, and Δt (s) is the discharge time.

RESULTS AND DISCUSSION

Material Structure and Morphology

The fabrication process of micro-mesoporous carbon is shown in **Figure 1**. This means *spirulina* extract impregnation makes the castor shell powder to form an internal wetting structure. The interaction of organic functional groups derived from castor shells and extracts under the catalysis of KOH was effective. Through condensation and dehydration reactions and so on, the nitrogen-rich organic group from *spirulina* extract

ISSN No. 2454-6194 | DOI: 10.51584/IJRIAS |Volume IX Issue VIII August 2024

infiltrated into castor shell particles, which confirms that distribution of KOH is more effective as activator to promote biomass carbonization to form interconnected networks micro-mesoporous materials by high temperature treatment in nitrogen atmosphere.

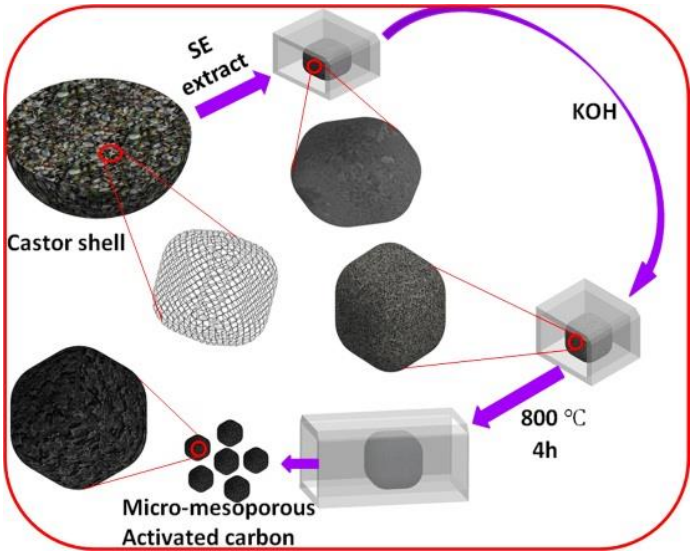

Figure 1 Nitrogen doped micro-mesoporous carbon fabrication process. SE: spirulina extract

Figure 2 a-i represents SEM image of the samples. The CSSK sample obtained by simultaneous decomposition and activation of *spirulina* extract impregnated castor shell powder with KOH activator, clearly shows some uniformly dispersed pores and interconnected network structure. In comparison, the CSS sample was prepared with castor shell powder as precursor containing the extract of *spirulina* without KOH, and it shows spherical particle stacking. Blocky particles with irregular appeared on CSK sample which was prepared without extract.

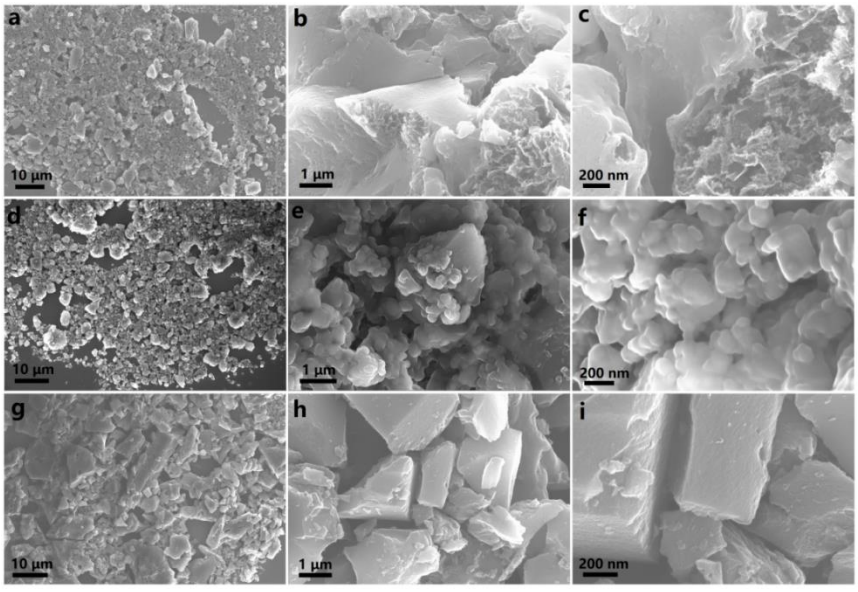

Figure 2 SEM images of all samples (a, b, c) CSSK, (d, e, f) CSS, (g, h, i) CSK

The TEM photos are shown in **Figure 3 a-c**. It is shown that there are overlaps between particles and some pores with nanoscale unique interconnected network structure on the sample CSSK. For the CSS sample, particles are densely with a few small holes and the CSK sample has a small amount of large pores. These results suggest that the extract can be impregnated inside of the castor shell powders for forming internal infiltrated structure, which may be beneficial to the interaction between the active agent KOH and the organic groups of biomass, and tends to form smaller micro-mesoporous texture under high temperature. This means that under the combined action of extract and KOH, the carbonization process of castor shell powder tends to

ISSN No. 2454-6194 | DOI: 10.51584/IJRIAS |Volume IX Issue VIII August 2024

be controlled to form more micro-mesoporous structures.

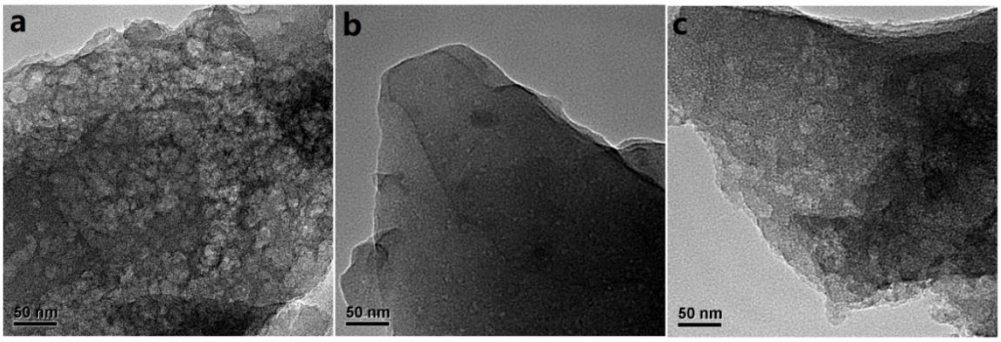

Figure 3. TEM images of all samples (a) CSSK, (b) CSS, (c) CSK

The XRD patterns of the obtained samples are displayed in **Figure 4 a**. It showed a broad peak at approximately 24°and a weak band at around 44°corresponding to the (002) and (100) planes, respectively, suggesting their typical amorphous graphitic structure. Obviously, it can be seen that the broad (002) diffraction peaks of CSK and CSSK samples are shifted to a low angle, which may be attributed to the activation process of KOH and the different surface doping amount of N and O heteroatoms of samples derived from biomass[22, 23]. The (100) peak intensity of CSSK and CSK is stronger than that of other samples, which is due to the activation with KOH, promoting the degree of graphitization. Further, Raman spectra of the samples are shown in **Figure 4 b**. Two peaks at 1344 cm^{-1} and 1592 cm^{-1} correspond to disordered and defective texture (D band) and graphitic structures (G band), respectively. The relative intensity ratio of G band to D band (I_G/I_D) represents the graphitization degree of carbon materials. The I_G/I_D of CSS, CSC, CSK and CSSK, is of 1.01, 1.04, 1.05, and 1.07, respectively with the gradual increase suggesting the enlargement of degree of graphitization which is highest in CSSK. These results are in good agreement with XRD analysis.

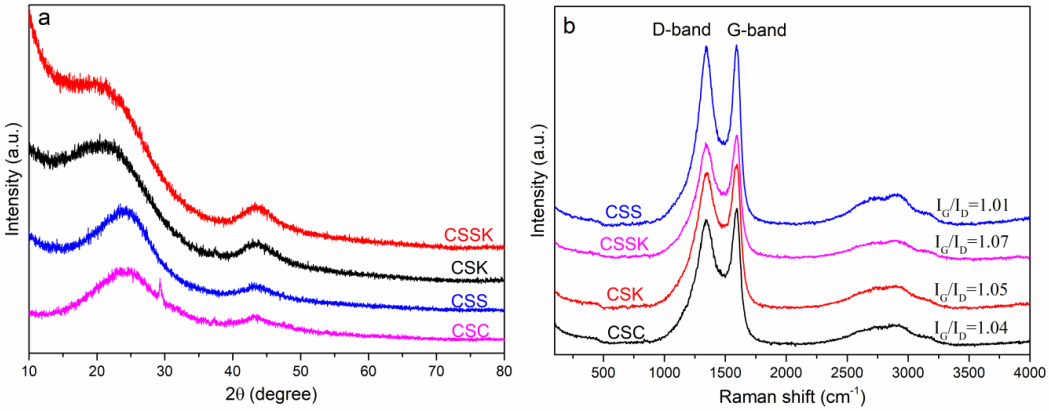

Figure 4 XRD pattern (a) and Raman spectra (b) of samples

Elemental analysis and infrared spectral data of *Spirulina* and castor shell powder are shown in **Table 1** and **Figure 5**, respectively. It can be seen that biomass contains inorganic salts and functional groups of carbohydrates and proteins. **Figure 6** shows FTIR spectra of samples pretreated with and without KOH at 40°C. The pure castor shell powder and *spirulina* extract in wave number 2000-500 cm^{-1} range are shown in the a and b curves, respectively. The infrared curve of the samples with KOH is shown as (c), (d) respectively. It can be seen from the curves that the peaks at 1442 cm^{-1} and 1160 cm^{-1} were disappeared, which may be attributed to the chemical interaction of KOH with COO^-, OH oxygen groups[24]. The new nearly 1330 cm^{-1} is due to O-C-O band. The peaks at 1655 cm^{-1} and 1550 cm^{-1} are due to amide I (C=O stretching vibration) and amide II (combination of C-N stretching vibration and N-H deformation vibration) from protein or polypeptide respectively[25.] This indicates that the interaction of amino group and carboxyl group of biomass catalyzed by KOH promotes the connection between biomass. Compared with the curve (c), except for the peak at 1659 cm^{-1}, the peaks shifted to lower wave number in the curve (d) indicate that the interaction between organic groups and KOH is enhanced. This means that the extracts of *spirulina* further react with the castor shell organic groups, forming an effective connection catalyzed by KOH. This could promote the formation of special

ISSN No. 2454-6194 | DOI: 10.51584/IJRIAS |Volume IX Issue VIII August 2024

micro-mesoporous structure in the further high temperature activation process.

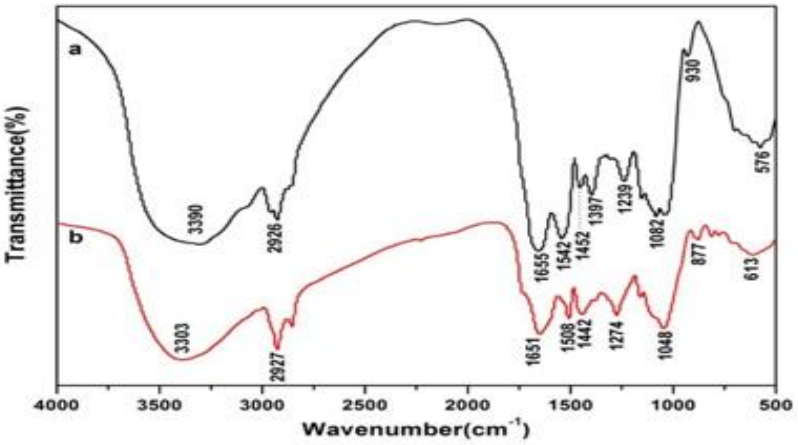

Figure 5 (a) Spirulina, (b) Castor seed shell

Table 1 EDS atomic percent data

	C (%)	O (%)	N (%)	K (%)	S (%)	P (%)	Na (%)	Cl (%)	Si (%)		
CSP	62.28	37.32	-	0.21	-	-	-	0.05	0.06	-	-
SE	56.03	27.49	15.10	0.28	0.14	0.15	0.64	0.11	0.04	-	-

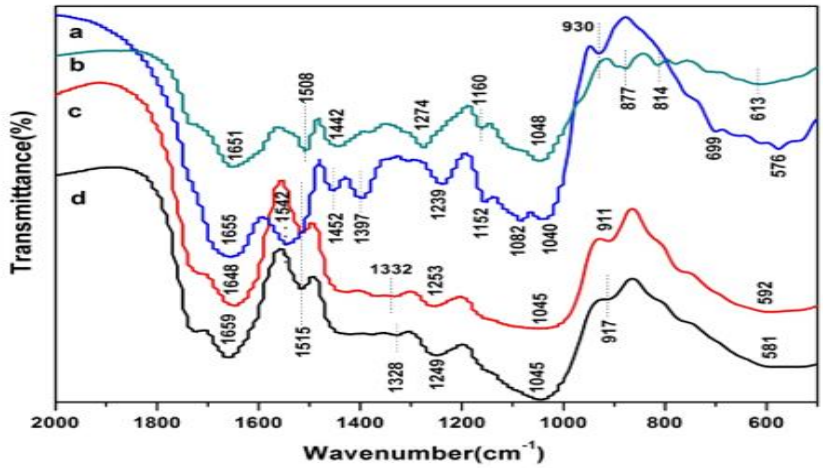

Figure 6. The infrared spectra of samples for (a) SE, (b) CSP, (c) CSP+KOH, (d) CSP+SE+KOH

FTIR result of samples treated with high temperature is represented as **Figure 7** for sample of CSC prepared from pure castor shell (CS) with calcination, the peak at 1405 cm^{-1} was assigned to C-OH bending vibration. The peak at 1042 cm^{-1} is assigned to C-O stretching vibration. The overall residual functional group of the CSC is small, indicating effective decomposition of large molecules or inorganic groups of pristine castor shell powder after treatment at 800 ℃. In comparison, other samples have new peaks. The peaks at 1673 and 1587 cm^{-1} are due to amide I (C=O stretching vibration) and amide II derived residues from biomass protein after high temperature treatment. The absorption peak at 1462 cm^{-1} corresponds to C-H bending vibration. The peak at 1405 cm^{-1} is due to O-H. The peaks at 1300 and 1059 cm^{-1} are attributed to C-O stretching vibration. The peaks at 1113 and 930 cm^{-1} are assigned to C-O-C stretching vibration. The peaks at 836, 767, 707, 664 and 622 cm^{-1} are assigned to C-H bending vibration. The peak at 530 cm^{-1} is assigned to M-O. The sample CSK shows O-H at 1636 cm^{-1} and C-H at 1384 cm^{-1} after KOH treatment. The peak at 1042 cm^{-1} is shifted to 1027 cm^{-1} and become stronger. The peak at 693 cm^{-1} is contributed to C-H[26]. For sample CSS, the peak at 1587 cm^{-1} is due to amide II. The peak at 1430 cm^{-1} is contributed to O-H. The peaks at 1087 and 1042 cm^{-1} are

ISSN No. 2454-6194 | DOI: 10.51584/IJRIAS |Volume IX Issue VIII August 2024

attributed to C-O stretching vibration. The peaks at 600 and 565 cm^{-1} are assigned to C-H and metal-O from metals in *spirulina* extract respectively. For sample CSSK, the amide II at 1587 cm^{-1} is maintained due to nitrogen doped porous carbons derived from *spirulina* extract. The weaker peak at 1405 cm^{-1} contributes to O-H. The peak at 1019 cm^{-1} is shifted from 1042 cm^{-1}, indicating additional source of oxygen perhaps one or more carboxylic acid form of the carbonyl[27]. The metal-O bonds were eliminated after KOH treatment. It may be attributed to the removal of inorganic groups with metal-O[28]. These results may be related to the interaction between extract of *spirulina* and castor shell. The complexes formed by metal ions and organic functional groups derived from the extracts, which promote the formation of the micro-mesoporous in the process of KOH activation.

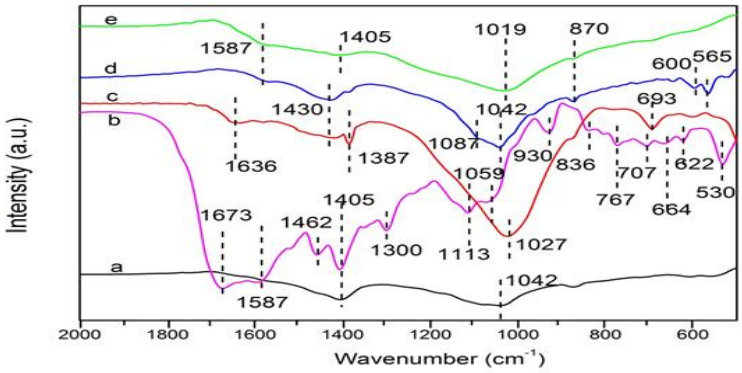

Figure 7. FTIR spectra of samples (a) CSC, (b) SE, (c) CSK, (d) CSS, (e) CSSK.

Figure 8 displays that the samples exhibit the typical type III N_2 adsorption-desorption isotherms according to the IUPAC classification with H3 hysteresis loop. All samples present the hysteresis loops at a relative pressure (P/P_0) range of 0.4–0.9, suggesting the presence of numerous small sized micropores and mesopores. The corresponding pore-size distribution curves demonstrated that the micro-mesopore sizes of CSK, CSS, and CSSK are 1.7–10.6 nm, 1.7–8.5 nm, and 1.8–13.7 nm, respectively. CSSK sample has more micropores and mesopores compared with other samples (see **Figure 8 f and Table 2**). The relative ratio of micropore to mesopore is more appropriate, which is conducive to the storage of ionic charges. The corresponding specific surface area are 891 $m^2 g^{-1}$ (CSK), 550 $m^2 g^{-1}$ (CSS) and 1527 $m^2 g^{-1}$ (CSSK), respectively (Table 1). This shows CSSK with highest specific surface area. The estimated total pore volume of CSK, CSS and CSSK is 0.431, 0.306 and 0.743 $cm^3 g^{-1}$, respectively. These results mean that sample CSSK has a rich micro-mesoporous texture and higher surface area. This phenomenon could be due to the fact that the interaction between extracts and castor shell powders which is favorable for KOH activator to form more effective micro-mesoporous structure at high temperature and coincides with the TEM results. This is conducive to the adsorption and transfer of charge on the surface of the electrode material for supercapacitor.

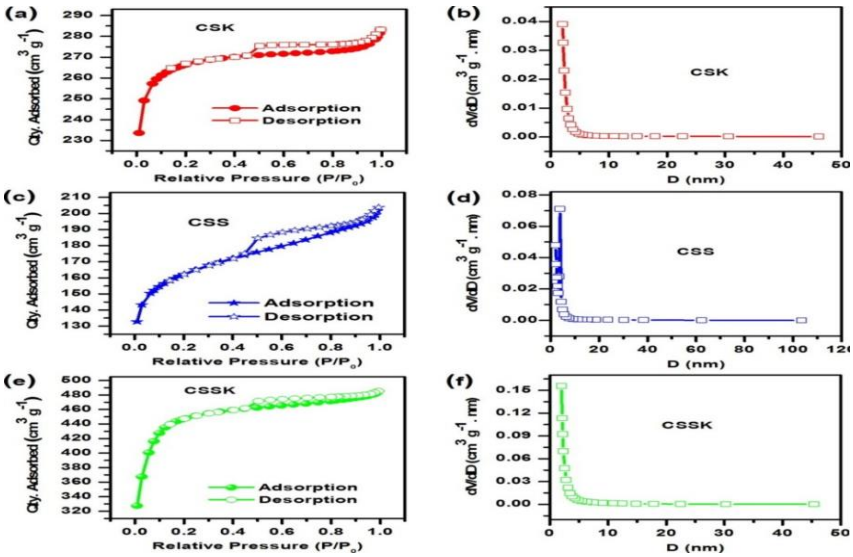

Figure 8 Nitrogen adsorption-desorption isotherms (a, c and e) and pore-size distribution (b, d, and f).

ISSN No. 2454-6194 | DOI: 10.51584/IJRIAS |Volume IX Issue VIII August 2024

Table 2 Porosity data of all samples

Sample	S_{BET} (m^2g^{-1})	V_{tot} (ml^3g^{-1})	V_{micro} (ml^3g^{-1})	V_{meso} (ml^3g^{-1})	V_{micro}/V_{tot}	D_{AC} (nm)
CSK	891	0.431	0.364	0.037	0.845	1.933
CSS	550	0.306	0.176	0.101	0.575	2.221
CSSK	1527	0.743	0.496	0.125	0.668	1.946

Sbet： BET specific surface area. V_{tot}: Total pore volume, V_{micro}: Micropore volume, V_{meso}: Mesopore volume, D_{AC}: Average pore size.

Figure 9 a shows the XPS energy spectrum of the samples. For oxygen, the binding energies around 530 eV, 531 eV, 532 eV and 533 eV represent C=O quinone type groups (O-I), C–OH phenol groups and/or C–O–C ether groups (O-II), and chemisorbed oxygen (COOH carboxylic groups) and/or water (O-III), respectively[29,30]. Compared with CSK and CSS, for CSSK samples, the fitting peak around 533 eV disappeared. New fitting peak around 530 eV was appeared which is attributed to the corresponding C=O chemical bonds. This may suggest that the removal of organic groups is more effective for CSSK samples in the process of activation promoting the increase of carbon content in the sample, which is conducive to the formation of the surface property of the sample to promote charge transfer. In addition, the interaction between extract and castor shell during high temperature activation facilitates the formation of carbon materials with micro-meso porous enhancing charge transport.

The N 1s spectra of samples are shown in **Figure 9 b**, the N 1s spectrum signal can be fitted into four sub-peaks, corresponding to pyridinic N (ca. 399.0 eV), pyrrolic N (ca. 399.7 eV), graphitic N (ca. 400.5 eV) and quaternary N (ca. 401.5 eV)[31]. It can be seen that nitrogen atoms with conjugated bonds on the skeleton of porous carbon at high temperatures were formed. Compared with CSK samples, the nitrogen spectrum peaks of CSS and CSSK samples with extract of *spirulina* shows shift to low binding energy, which means the density of electronic cloud be increased with electron donating properties. This has significant benefits to improve the charge transfer rate and CSSK is expected to own the best capacitance performances.

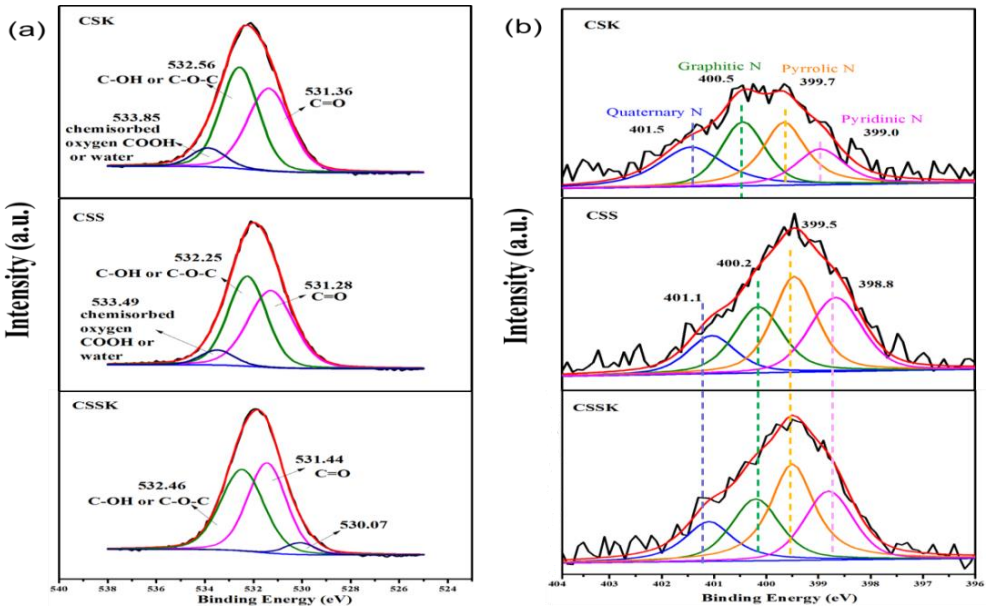

Figure 9. XPS survey spectra of samples (a) O1s spectra, (b) N1s spectra

Elemental analysis was performed to determine the chemical compositions of the raw material, activated samples with and without *spirulina*. The results in **Table 3** show that the carbon content of samples increases by high temperature activation, while the amount of heteroatoms decreases compared with that of raw materials. The sample CSSK has a moderate carbon content of 72.15 % compared to the sample CSC 75.95 %,

CSS 53.65 %, CSK 83.48 % and higher doped nitrogen of 1.83 % than CSC 1.16 %, CSS 1.13 %, CSK 0.62 %. Therefore, based on the results, the existence of heteroatoms can improve the hydrophilicity/wettability of the carbon surface to electrolyte and thus increase the electrochemical activity and good cycle stability.

Table 3. Elemental analysis of castor shell derived porous carbons.

samples	C (%)	H (%)	N (%)	O[a] (%)
SE	40.33	9.23	9.53	40.91
CS	48.18	9.87	1.13	40.82
CSC	75.95	3.46	1.16	19.41
CSS	53.65	6.28	1.13	38.94
CSK	83.48	1.97	0.62	13.93
CSSK	72.15	3.36	1.83	22.66

O[a] is estimated by difference. SE: spirulina extract; CS: castor shell; CSC: castor shell carbon; CSS: spirulina-mixed castor shell carbon; CSK: KOH-mixed castor shell carbon; CSSK: spirulina-KOH mixed castor shell carbon

Electrochemical Performance

The capacitive performance of as-prepared materials was evaluated by using cyclic voltammetry (CV), galvanostatic charge–discharge (GCD), and electrochemical impedance spectroscopy (EIS) techniques in 6.0 M KOH aqueous solution in a three-electrode system. The cyclic voltammograms are shown in **Figure 10 a**. Based on a fixed potential window (- 0.5 -0.2 V) and constant scan rate of 20 mV s^{-1}. All the as-prepared samples present an approximately rectangular CV shape, suggesting an ideal double-layer capacitance based on ionic adsorption and desorption. It can be seen clear that the CV curve of the CSSK electrode exhibits a larger area than other electrodes, indicating it has a highest specific capacitance. **Figure 10 b, c, and d,** present the CV curves of samples at scan rates from 20 to 100 mV s^{-1} and the rectangle-like shapes of CV were observed without large distortion even at 100 mV s^{-1}. Compared with CSS and CSK sample electrodes, the CSSK electrode quasi-rectangles are consistently with high current densities. It implies that the CSSK sample has fast kinetics for EDLC formation over the surface of micro-mesoporous carbons, which should improve rate capacity and stability[32].

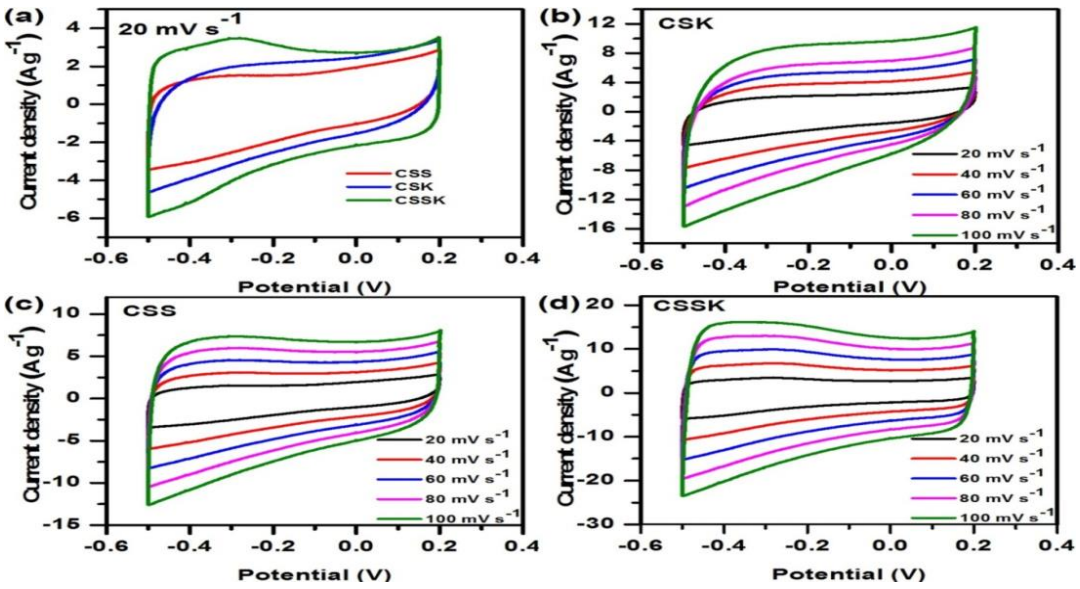

Figure 10. (a) CV curves of CSK, CSS, and CSSK, (b), (c), and (d) corresponding consistent quasi-rectangle test with varied scan rate.

ISSN No. 2454-6194 | DOI: 10.51584/IJRIAS |Volume IX Issue VIII August 2024

Figure 11 a, shows the galvanostatic charge-discharge curves of different samples at 1.0 A g^{-1}. All samples display symmetrically shaped GCD curves, indicating a high degree of the reversibility for charge storage and delivery[33]. Correspondingly, the GCD curves of electrodes of CSK, CSS, and CSSK at various current densities are shown in **Figure 11 b, c and d**, respectively. The corresponding specific capacitance was calculated based on the galvanostatic charge-discharge method, and the correlation between the specific capacitances. The CSSK electrode shows excellent specific capacitance of 333 F g^{-1} at a current density of 1.0 A g^{-1}, which is significantly higher than that of CSK (243 F g^{-1}) and CSS (151 F g^{-1}).

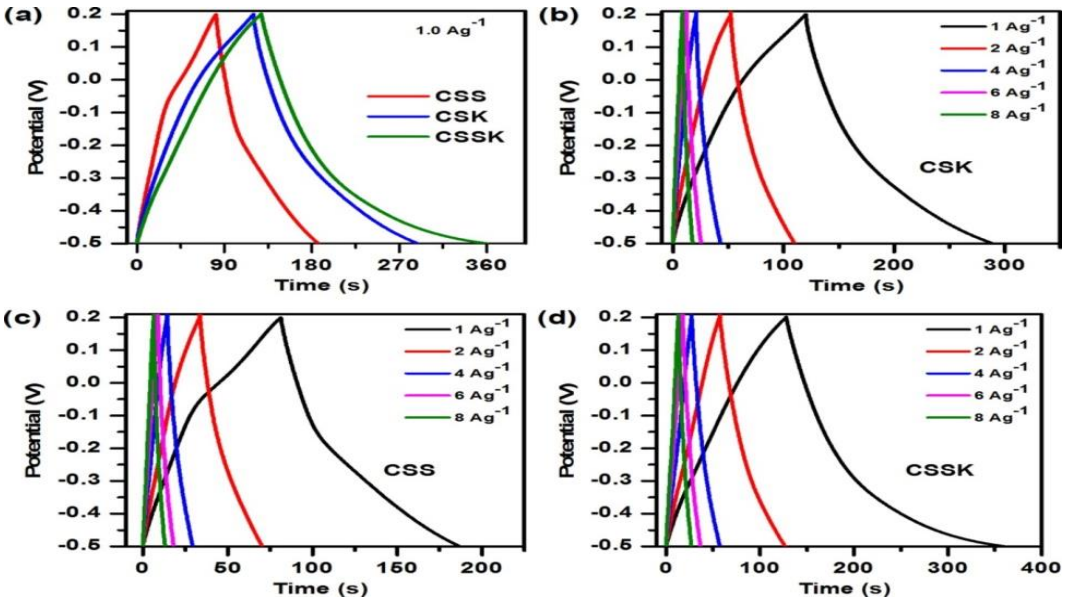

Figure 11 (a) GCD curves of CSK, CSS, and CSSK at 1 A g^{-1}, (b, c, d) consistent charge-discharge test at different current densities

The data related to electrode performance of the three electrode system are shown in **Figure 12**. As seen from **Figure 12 a**, with the increase of current density, the specific capacitance of the electrode is decreasing gradually. In comparison, the specific capacitance of CSSK electrode decreases slowly in range of 10-20 A g^{-1} current density of three electrodes. Even at a high current density of up to 20 A g^{-1}, CSSK still exhibits a superior specific capacitance of 138.43 F g^{-1}, while CSK and CSS are 84.86 and 64.27 F g^{-1}, respectively. The excellent rate capability of CSSK could be due to the effective ion diffusion channels and nitrogen doping improved hydrophilicity/wettability in micro-mesoporous carbon. Capacitance cycle stability graph is shown in **Figure 12 b**. After 10,000 cycles at 10 A g^{-1} CSSK still retains 99.7 % of the initial capacitance, indicating maintained structural pores stable. The preserved nitrogen doped interconnected networks micro-mesoporous carbon with *spirulina* allows for unobstructed electron and ion transport within the composites, thereby generating reversible capacitive behavior even at high charging/discharging rates.

The electrochemical impedance spectroscopy (EIS) of samples was employed in 6 M KOH solution at a frequency range from 0.01 Hz to 10 KHz under amplitude potential of 5 mV yields the Nyquist plots. **Figure 12 c** shows Nyquist plots of the as-prepared CSK, CSS, and CSSK electrodes. The electrolytic contact resistance and the charge transfer resistance are identified at high frequency region, the intercept on real axis, while the mass transfer resistance is identified by Warburg at low frequency region, all differs for each sample.

Each of their EIS data was fitted, simulated in accordance with the equivalent circuit (**Figure 12 c**, **and Table 4**), with the three components. The EIS Nyquist plots exhibit small semicircle in the high frequency region related to charge transfer resistance (Rct), 45°Warburg section in the middle frequency region (Warburg impedance Zw) associated with the porous structure of the electrode, double-layer capacitance (C_{dl}) and pseudocapacitive element (C_l)[34]. At very high frequency, the intercept on X-axis represents a combined internal resistance (Rs) of electrolyte solution resistance, intrinsic resistance of active materials and interfacial contact resistance of active materials and current collectors[35]. From the data of Table S2 equivalent circuit simulation, it can be seen that Rs of CSK, CSS and CSSK is 0.64, 0.77 and 0.53 ohms respectively, the corresponding, Rct is 0.69, 0.70, 0.55 ohms respectively. These consistent lowest values of mass transfer resistances coincided

ISSN No. 2454-6194 | DOI: 10.51584/IJRIAS |Volume IX Issue VIII August 2024

with shortened ion diffusion distance in modified abundant networked micro-meso pores structure. This observation implies that the CSSK sample has a low diffusion resistance in the pores, indicating the good electrical properties of the material. When considered that CSK performance is better than CSS, the decomposed functional carbon-carbon at interface of spirulina extract and castor shell had significant role, much better in presence of the KOH activator responsible for better performance of CSSK.

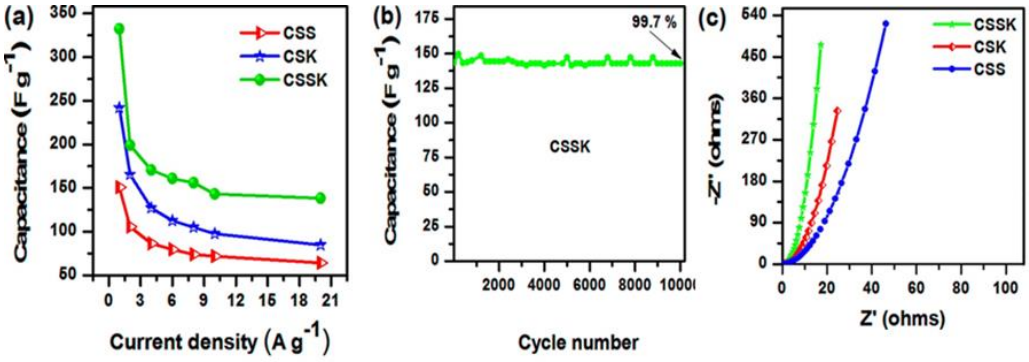

Figure 12 (a) varied specific capacitance at varied current density calculated from GCD curves, (b) cycling stability of CSSK-based supercapacitor upon charging/discharging at constant current density of 10 A g^{-1}, (c) EIS Nyquist plot of CSK, CSS, and CSSK

Table 4. Summary of circuitry components

Samples	Rs (ohm)	Rct (ohm)	Zw (ohm)	C_{dl} (Farad)	C1 (Farad)
CSK	0.64	1.34	0.122	0.0012	0.035
CSS	0.77	1.54	0.177	0.0017	0.051
CSSK	0.53	0.88	0.062	0.0009	0.033

Figure 13 a, b and c show the corresponding GCD curves of the samples supercapacitor at different current densities, demonstrating nearly symmetric triangle shapes for all current densities from 1 to 3 A g^{-1}. Cyclic voltammetry curves of two-electrode system in same 6M KOH from 0 to 1.2 V when scan rate is 20 mV s^{-1} is shown in **Figure 14**. All the as-prepared samples present an approximately rectangular CV shape indicating the behavior of an electrical double-layer capacitor. It can be seen clear that the CV curve of the CSSK electrode exhibits a larger area than other electrodes, suggesting it has a highest specific capacitance.

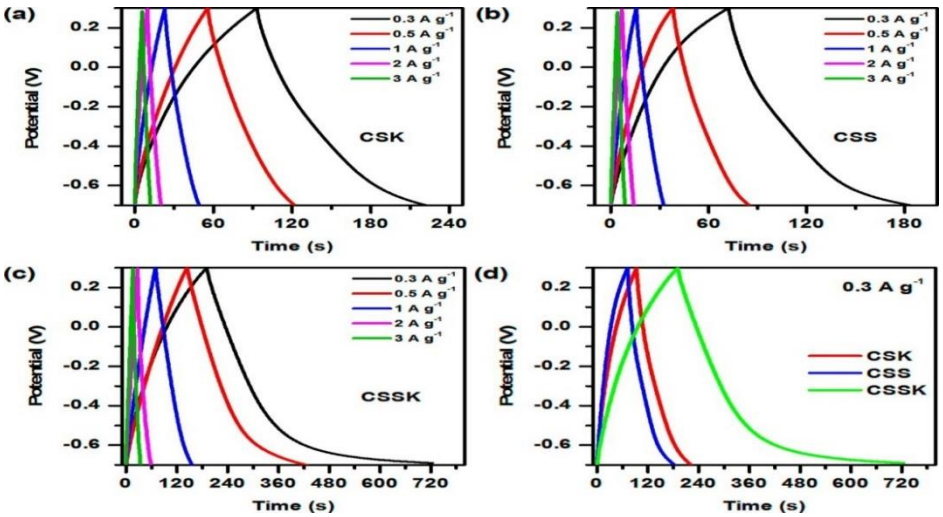

Figure 13 Two-electrode system GCD repeated at varied current density (a-c), and compared CSK, CSS, and CSSK at low current density (d). The specific capacitance at 0.3 A g-1.

ISSN No. 2454-6194 | DOI: 10.51584/IJRIAS |Volume IX Issue VIII August 2024

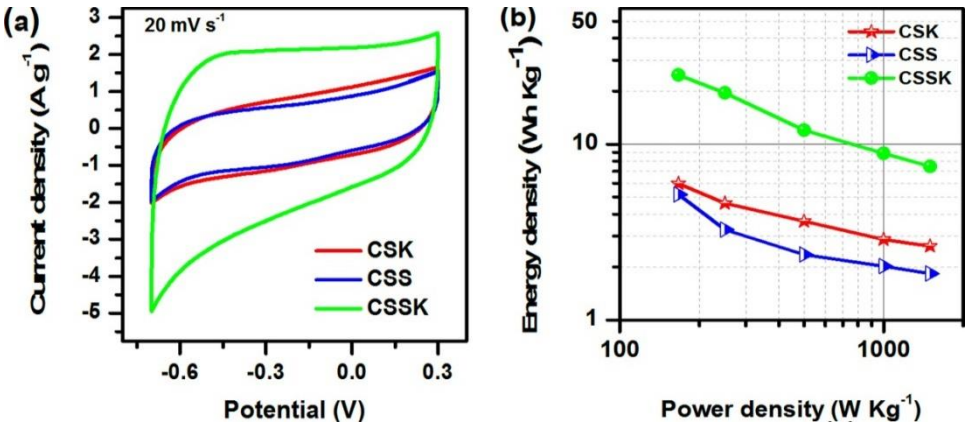

Figure 14. (a) Cyclic voltammetry curves of two-electrode system in same 6M KOH from -0.7 to 0.3 V when scan rate is 20 mV s^{-1}, (b) Ragone plots of energy verses power of two-electrode system

In order to compare energy density of CSSK electrode to other biomass-derived carbons electrode, Fig. 10a and 10b show two-electrode configuration GCD and CV results. The GCD curves of the two-electrode configuration at various current densities from 1 to 5 A g^{-1} (**Figure 15 a**). In addition, it can be obtained from the **Figure 15 a** that the specific capacitance of the two-electrode configuration is 50, 40.8, 37, 36.6 and 32 F g^{-1} at 1, 2, 3, 4 and 5 A g^{-1}, respectively. **Figure 15 b** shows that the shape of the CV curves does not change significantly as the scan rate increases, indicating a good fast charge and discharge performance for two-electrode configuration. The result in **Figure 15 c** produced both high energy and power densities as nitrogen doped biomass-derived carbon. The CSSK maintained high energy density of 10 Wh kg^{-1} at a power density of 600 W kg^{-1} and energy density of 8.2 Wh kg^{-1} at a power density of 1200 W kg^{-1}, still remains 6.4 Wh kg^{-1} at a power density of 3000 W kg^{-1}. This excellent performance is significantly higher than the previously reported literatures[36-39] such as activated biomass carbon made from bamboo (10.9 Wh kg^{-1} at 63 W kg^{-1}), bio-based nitrogen- and oxygen-doped porous carbon derived from cotton (9.95 Wh kg^{-1} at 236 W kg^{-1}), nitrogen-doped porous activated carbon for supercapacitor derived from pueraria (8.46 Wh kg^{-1} at 123 W kg^{-1}) and heteroatom-doped porous carbons derived from moxa floss(10 Wh kg^{-1} at 70.3 W kg^{-1}) (as summaries in **Table 5**).The cyclability of the symmetric supercapacitor displays 91.7 % capacitance retention after 10000 cycles at 5 A g^{-1} (**Figure 15 d**), demonstrating excellent electrochemical cyclability. It can be seen from the above comparison, the performance of two-electrode configuration is superior. Considering that the renewable microalgae and bio-carbon source, simple preparation method and low cost as well superior performance, the CSSK has great potential in carbon materials for supercapacitor.

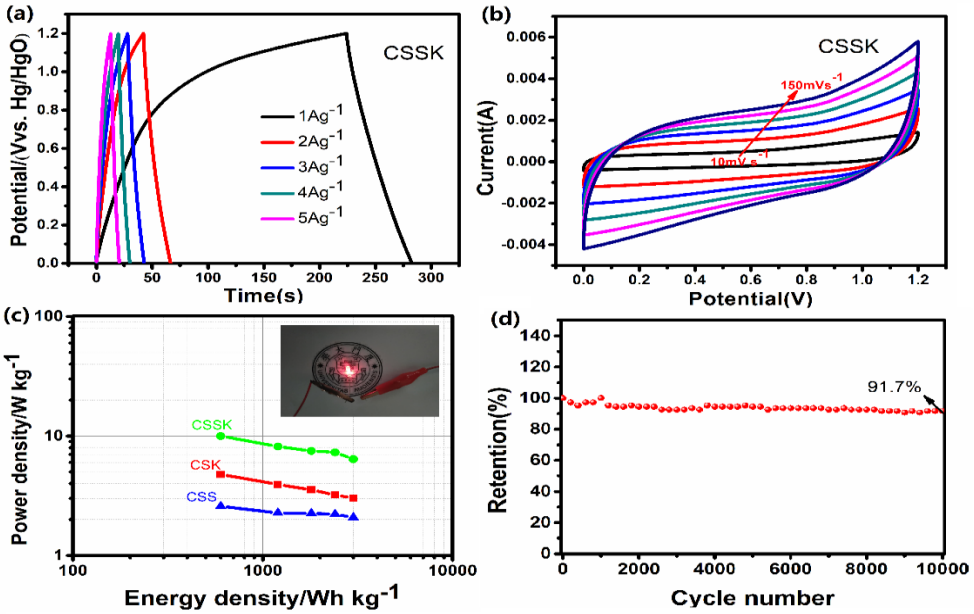

Figure 15. Two-electrode system GCD of CSSK at varied current densities (a), CV at varied scan rate (b), Ragone plot of symmetric supercapacitor(c), Cycling performance at a current density 5 A g^{-1}(d)

ISSN No. 2454-6194 | DOI: 10.51584/IJRIAS |Volume IX Issue VIII August 2024

Table 5 Electrochemical performance of carbon-based supercapacitors

Biomass precursor	**Electrolyte**	**Energy density (Wh kg^{-1})**	**Power density (W kg^{-1})**	**References**
bamboo	3 M KOH	10.9	63	40
cotton	0.5 M Na_2SO_4	9.95	236	41
shengli lignite	6 M KOH	8.11	90	42
argy wormwood	6 M KOH	8.1	480	43
sugar cane bagasse	1 M H_2SO_4	10	-	44
spirulina mediated castor shell	6 M KOH	10	600	This work

Cost Analysis and Life Cycle Assessment

Usually, due to the conventional synthesis processes, carbon materials lack surface modified nitrogen. The nitrogen functional groups present on the carbon materials generally existed by direct synthesis from a nitrogen-containing precursor or by post-treatments of the material with a nitrogen-containing reactant, such as NH_3 and HCN [45]. **Figure 16** summarizes the main nitrogen groups found on the surface of carbon materials [45].

The global production of ammonia (NH_3) was estimated as being 160 million tons in 2020 (147 tons of fixed nitrogen) [46]. China accounted for 26.5% of that, followed by Russia at 11.0%, the United States at 9.5%, and India at 8.3% [46]. In particular the extra cost of producing ammonia from urea and calcium hydroxide or through Harber process involving atmospheric nitrogen (N_2) and hydrogen (H_2), compared with the direct use of bio-source nitrogen precursor, deters frequent use of ammonia as nitrogen-doping source. Other preparation methods such as adding acid to cyanide salt of alkaline metals and using Andrussow oxidation to produce nitrogen cyanide still add to the cost than the direct synthesis with the bio-source nitrogen precursor.

The nitrogenous materials in *Spirulina* include the amino acids that readily involve in breakdown of peptide bonds for effective nitrogen-doping. More amino groups are also available during the breakdown of the peptide bonds in pyrolysis to favor carbon surface modification. *Arthrospira Platensis* type used in the self-nitrogen doped mesoporous carbon is autotrophic, meaning that it is able to make its own food, and do not need a living energy or organic carbon source. This type of *Spirulina* commonly grows anytime of the seasons making the nitrogen source cost effective and no further cost is required to prepare the nitrogenous group for doping process.

In practice, 500g *Arthrospira Platensis* (*Spirulina* powder) costs 26 US dollar and only 2 g was used to produce 13 times the nitrogenous extract used in doping the carbon. Thus, the cost of the nitrogenous extract contributed only 0.4 % to the total cost of the *Spirulina*, cheaper than the ammonia gas source of nitrogen usually flown at 100 cm^3/min. throughout the pyrolysis time. The ammonia gas fed at continuous rate for 4 hrs. contributed 48 % cost to the total cost of 50 L of ammonia gas. Thus, the bio-source based *Spirulina* provided a cheaper process and high availability of nitrogenous amino acids.

However, the cost of chemical potassium hydroxide still remains general challenge in preparing mesoporous carbon. In this work the glutenous property of arginine in *Spirulina* was explored and only small amount of potassium hydroxide was used in the pyrolysis for ionic intercalation purposes and indirectly reduced the total cost of KOH used.

ISSN No. 2454-6194 | DOI: 10.51584/IJRIAS |Volume IX Issue VIII August 2024

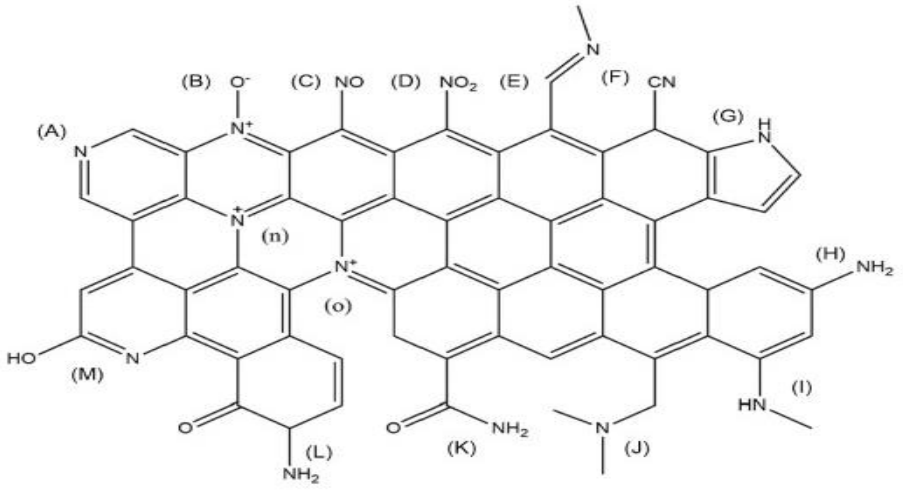

Figure 16. Nitrogen functional groups present on the surface of carbon materials: (A) pyridine, (B) N-oxidized pyridine, (C) nitrosyl, (D) nitro, (E) imine, (F) nitrile, (G) pyrrole, (H) primary amine, (I) secondary amine, (J) tertiary amine, (K) amide, (L) lactam, (M) pyridone, (N) quaternary nitrogen at the basal plane, and (O) quaternary nitrogen at the edge of the layer.

For life cycle assessment, the inventory collection of materials in Table 6 lists material information about the synthesis process.

Table 6. List of material and relevant information

Material name	Units	Material quantity
Spirulina powder	gram	2
Deionized water	ml	50
Castor shell powder	gram	2
Spirulina extract	ml	4
Potassium hydroxide solution	ml	2

Table 7. Scenario descriptions for materials by life cycle stage

Life cycle module	**Material scenarios**				
	***Spirulina* powder**	**Deionized water**	**Castor shell powder**	***Spirulina* extract**	**KOH solution**
A4: Transport	Transport materials from grocery store to the laboratory				
A5: Construction/synthesis	1. Incubate *Spirulina* powder for 4 hrs. @ 200 degrees Celsius in an electric oven with 15 min of preheating. 2. Extract the *Spirulina* solution by filter in beaker. No additional energy beyond human labor is needed. 3. Pyrolysis of *spirulina* extract mixed castor shell powder and KOH for 4 hrs. @800 degree Celsius. 4. Waste: Solution that originally contained the soluble salt ingredients (materials) is disposed in the drainage.				

ISSN No. 2454-6194 | DOI: 10.51584/IJRIAS |Volume IX Issue VIII August 2024

	5. Water use: Assume that 1 gallon of deionized, unheated water is used to clean the mixing and experimental devices.				
B1: Use	Smell of *Spirulina* extract and castor shell powder in general will be emitted into surrounding environment. Assume that these smells have a negligible environmental impact. Occasional cleaning may be required, but environmental impact of cleaning is ignored due to lack of data and method to report.				
B4: Replacement	No replacement needed for *Spirulina* powder	No replacement needed for deionized water	No replacement needed for castor shell	*Spirulina* extract replaced 1 time	Potassium hydroxide replaced 1 time
C2: Transport	Transportation to the drainage facility will be performed by a collection piping over a distance of 20 miles				KOH will be taken by collection pipe to the recycling facility, over a distance of 10 miles.
C4: Disposal	At the recycling facility, the remains of the soluble salt will join the stream feedstock, which will be allowed to transform under ideal conditions				Not applicable (final product will be used to make new KOH)

The environmental impact factors used for this synthesis process are shown in Table 8 and considers global warming potential (GWP) as the only environmental impact measure. Note that the energy taken to raise *Spirulina* powder to 20 ℃ is 0.00002324 Kwh and 0.000928 Kwh for raising castor shell/Spirulina extract/KOH mixture to 800 ℃ . At 4 hours total of 0.00009296 Kwh and 0.003712 Kwh were spent to release CO2 from spirulina powder and castor shell powder/spirulina extract/KOH mixture respectively. The emission factor for biomass used is generally considered as 0.0249 kg CO_2/Kwh. Thus, the potential release of CO_2 to environment can be calculated.

CO_2 emission = total energy (Kwh) * emission factor (kg CO_2/Kwh) * (1 - ER/100)

Where ER is the emission reduction efficiency approximately 98% desired.

Only two materials undergoing heating: *Spirulina* powder for extract and castor shell powder/*Spirulina* extract/KOH mixture are considered for the environmental impact factor.

Table 8. Environmental impact factors of materials

Material	**Units**	**Global warming potential [kg CO2e/unit of material]**			
		Production stage (A1-A3)	**Construction stage (A4-A5)**	**Use stage (B1-B7)**	**End-of-life stage (C1-C4)**
Spirulina powder for extract	gram	$2.315 * 10^{-6}$	No additional energy beyond human labor is	under module B4: Replacement, which is within the Use stage is	$1.158 * 10^{-7}$

ISSN No. 2454-6194 | DOI: 10.51584/IJRIAS |Volume IX Issue VIII August 2024

			needed	calculated below	
Castor shell powder/*Spirulina* extract/KOH mixture	gram	$9.243 * 10^{-5}$	No additional energy beyond human labor is needed	under module B4: Replacement, which is within the Use stage is calculated below	$4.622 * 10^{-6}$

The carbon material will have to be replaced over the required service life (and RSP) of 1250 days for supercapacitors. The number of replacements required for the Use stage:

For electrode carbon bonded with polytetrafluoroethylene (PTFE), its life span is 416 days. Only 2 gram of the carbon mixture was used. After the initial installation, the carbon mixture will have been replaced two times over the 1250 days required service life of the supercapacitor LCA.

Number of replacements required

= (1250 days) / (416 days life span) – 1 instance for initial installation

= 3.005 – 1

= 2 replacements

Total quantity of carbon mixture to be replaced = (2 gram) * (2 replacements) = 4 gram

Now we can apply the environmental impact factors from Table 8 to the material quantities.

The Use stage will need to include the production and end-of-life stage impacts.

Global warming potential, GWP of production stage = ($2 * 10^{-5}$ kg) * ($9.243 * 10^{-5}$ kg CO2e/kg)

= $1.849 * 10^{-5}$ kg CO2e

GWP of Use stage = ($4 * 10^{-5}$ kg) * [($9.243 * 10^{-5}$ kg CO2e from product stage + $4.622 * 10^{-6}$ kg CO2e from end-of-life stage)/ kg]

= ($4 * 10^{-5}$ kg) * ($9.243 * 10^{-5}$ + $4.622 * 10^{-6}$)

= $3.882 * 10^{-9}$ kg CO2e

GWP of end-of-life stage = ($2 * 10^{-5}$ kg) * ($4.622 * 10^{-6}$ kg CO2e/kg)

= $9.244 * 10^{-11}$ kg CO2e

The final global warming potential results for the synthesis process and life cycle stages are shown in Table 9.

Table 9. Global warming potential results by life cycle stage

Material	**Global warming potential [kg CO2e]**			
	Production stage (A1-A3)	**Construction stage (A4-A5)**	**Use stage (B1-B7)**	**End-of-life stage (C1-C4)**
Castor shell powder/*Spirulina* extract/KOH mixture	$1.849 * 10^{-5}$	No additional energy beyond human labor is needed	$3.882 * 10^{-9}$	$9.244 * 10^{-11}$

ISSN No. 2454-6194 | DOI: 10.51584/IJRIAS |Volume IX Issue VIII August 2024

CONCLUSION

Herein, novel extract of *spirulina* was infiltrated into the castor shell powder as precursor. Extract of *spirulina* contained nitrogen-rich mediated KOH activation of castor shell. The modified particles were activated at high temperature to form a unique nitrogen doped micro-mesoporous structure material (CSSK) with higher specific surface area of 1527 $m^2 g^{-1}$ compared with that of castor shell without spirulina extract as precursor. CSSK showed enhanced electrochemical behaviors, and the capacitance is up to 333 F g^{-1} at 1 A g^{-1}. Further charge/discharge cycling behavior shows only loss of 0.3 % of total capacity for CSSK after 10,000 cycles at a current load of 10 A g^{-1}. The as-prepared sample promotes transfer of charge and reduction of resistance, improves mass kinetics of electrolytic supercapacitor. This symmetric supercapacitor (CSSK) has demonstrated a remarkable energy density of 10 Wh kg^{-1} at a power density of 600 W kg^{-1} and good cycling behavior (after 10000 cycles 91.7 % retention of specific capacitance). These results will contribute to development of modified biomass carbon derived from biomass extracts for carbon electrode materials.

REFERENCES

1. Wang J, Nie P, Ding B, Dong S, Hao X, Dou H, et al., Biomass derived carbon for energy storage devices, J. Mater. Chem. A 5 (2017) 2411-2428.
2. Deng J, Li M, Wang Y, Biomass-derived carbon: synthesis and applications in energy storage and conversion, Green Chem. 18 (2016) 4824-4854.
3. Purkait T, Singh G, Singh M, Kumar D, Dey R.S. Large area few-layer graphene with scalable preparation from waste biomass for high-performance supercapacitor, Sci Rep 7 (2017).
4. Liu S, Zhao Y, Zhang B, Xia H, Zhou J, Xie W. et al., Nano-micro carbon spheres anchored on porous carbon derived from dual-biomass as high rate performance supercapacitor electrodes, J. Power Sources 381 (2018) 116-126.
5. Zhang Y, Liu X, Wang S, Li L, Dou S. Bio-Nanotechnology in High-Performance Supercapacitors, Adv. Funct. Mater. 7 (2017) 1700592.
6. Wu Y, Cao J.-P, Zhao X.-Y, Hao Z.-Q, Zhuang Q.-Q, Zhu J.-S. et al., Preparation of porous carbons by hydrothermal carbonization and KOH activation of lignite and their performance for electric double layer capacitor, Electrochim. Acta 252 (2017) 397-407.
7. Shao J, Ma F, Wu G, Dai C, Geng W, Song S. et al., In-situ MgO ($CaCO_3$) templating coupled with KOH activation strategy for high yield preparation of various porous carbons as supercapacitor electrode materials, Chem. Eng. J. 321 (2017) 301-313.
8. Dai C, Wan J, Yang J, Qu S, Jin T, Ma F. et al., H_3PO_4 solution hydrothermal carbonization combined with KOH activation to prepare argy wormwood-based porous carbon for high-performance supercapacitors, Appl. Surf. Sci. 444 (2018) 105-117.
9. Su X.-L, Cheng M.-Y, Fu L, Yang J.-H, Zheng X.-C, Guan X.-X. Superior supercapacitive performance of hollow activated carbon nanomesh with micro-meso structure derived from poplar catkins, J. Power Sources 362 (2017) 27-38.
10. Liang Y, Cao Q, Zheng M, Huo H, Hu H, Dong H. et al., Teflon: A Decisive Additive in Directly Fabricating Micro-meso Porous Carbon with Network Structure from Natural Leaf, ACS Sustain. Chem. Eng. 5 (2017) 9307-9312.
11. Zhao G, Chen C, Yu D, Sun L, Yang C, Zhang H. et al., One-step production of O-N-S co-doped three-dimensional micro-meso porous carbons for high-performance supercapacitors, Nano Energy 47 (2018) 547-555.
12. Ma G, Yang Q, Sun K, Peng H, Ran F, Zhao X. et al., Nitrogen-doped porous carbon derived from biomass waste for high-performance supercapacitor, Bioresour. Technol. 197 (2015) 137-142.
13. Feng S, Li W, Wang J, Song Y, Elzatahry A. A, Xia Y. et al., Hydrothermal synthesis of ordered mesoporous carbons from a biomass-derived precursor for electrochemical capacitors, Nanoscale 6 (2014) 14657-14661.
14. Dutta S, Bhaumik A, Wu K.C.W. Micro-mesoly porous carbon derived from polymers and biomass: effect of interconnected pores on energy applications, Energy Environ. Sci. 7 (2014) 3574-3592.
15. Cheng B.H, Zeng R.J, Jiang H. Recent developments of post-modification of biochar for electrochemical energy storage, Bioresour. Technol. 246 (2017) 224-233.

16. Sun J., Niu J., Liu M., Ji J., Dou M., Wang F., Biomass-derived nitrogen-doped porous carbons with tailored micro-meso porosity and high specific surface area for high energy and power density supercapacitors, Appl. Surf. Sci. 427 (2018) 807-813.
17. Gao Y, Zhang W, Yue Q, Gao B, Sun Y, Kong J. et al., Simple synthesis of micro-meso porous carbon from Enteromorpha prolifera by a self-template method for supercapacitor electrodes, J. Power Sources 270 (2014) 403-410.
18. Kumar K.V, Gadipelli S, Preuss K, Porwal H, Zhao T, Guo Z.X. et al., Salt Templating with Pore Padding: Micro-meso Pore Tailoring towards Functionalised Porous Carbons, ChemSusChem 10 (2017) 199-209.
19. Gao S, Tang Y, Wang L, Liu L, Sun Z, Wang S. et al., Coal-Based Micro-meso Porous Carbon Synthesized with a Soluble Salt Self-Assembly-Assisted Method for High Performance Supercapacitors and Li-Ion Batteries, ACS Sustain. Chem. Eng. 6 (2018) 3255-3263.
20. Li H, Liu Z, Zhang Y, Li B, Lu H, Duan N. et al., Conversion efficiency and oil quality of low-lipid high-protein and high-lipid low-protein microalgae via hydrothermal liquefaction, Bioresour. Technol. 154 (2014) 322-329.
21. Wang Q, Li Y, Wang K, Zhou J, Zhu L, Gu L. et al., Mass production of porous biocarbon self-doped by phosphorus and nitrogen for cost-effective zinc–air batteries, Electrochim. Acta 257 (2017) 250-258.
22. Zhang X, Niu Q, Guo Y, Gao X, Gao K, Heteroatom-doped porous carbons derived from moxa floss of different storage years for supercapacitors, RSC Advances 8 (2018) 16433-16443.
23. Li Y, Zheng K, Ali Shah S.A, Huang Y, Tian Y, Cheng J. et al., Winter-jujube-derived carbon with self-doped heteroatoms and a micro-mesoly porous structure for high-performance supercapacitors, RSC Advances 7 (2017) 43356-43365.
24. Zhang X, Zhang L, Li A. Eucalyptus sawdust derived biochar generated by combining the hydrothermal carbonization and low concentration KOH modification for hexavalent chromium removal, J. Environ. Manage. 206 (2018) 989-998.
25. Fang L, Zhou C, Cai P, Chen W, Rong X, Dai K. et al., Binding characteristics of copper and cadmium by cyanobacterium Spirulina platensis, J. Hazard. Mater. 190 (2011) 810-815.
26. Kataki S, Hazarika S, Baruah D.C. Investigation on by-products of bioenergy systems (anaerobic digestion and gasification) as potential crop nutrient using FTIR, XRD, SEM analysis and phyto-toxicity test, J. Environ. Manage. 196 (2017) 201-216.
27. Kothari R, Prasad R, Kumar V, Singh D.P. Production of biodiesel from microalgae Chlamydomonas polypyrenoideum grown on dairy industry wastewater, Bioresour. Technol. 144 (2013) 499-503.
28. Romanos J, Beckner M, Stalla D, Tekeei A, Suppes G, Jalisatgi S. et al., Infrared study of boron–carbon chemical bonds in boron-doped activated carbon, Carbon 54 (2013) 208-214.
29. Zhou M, Li X, Zhao H, Wang J, Zhao Y, Ge F. et al., Combined effect of nitrogen and oxygen heteroatoms and micropores of porous carbon frameworks from Schiff-base networks on their high supercapacitance, J. Mater. Chem. A 6 (2018) 1621-1629.
30. Lu C, Wang D, Zhao J, Han S, Chen W. A Continuous Carbon Nitride Polyhedron Assembly for High-Performance Flexible Supercapacitors, Adv. Funct. Mater. 27 (2017) 1606219.
31. Yu S, Zhu X, Lou G, Wu Y, Xu K, Zhang Y. et al., Sustainable micro-meso porous biomass carbons enriched with pyridinic and pyrrolic nitrogen for asymmetric supercapacitor, Mater. Design 149 (2018) 184-193.
32. Yin L, Chen Y, Li D, Zhao X, Hou B, Cao B. 3-Dimensional micro-meso porous activated carbon derived from coconut fibers with high-rate performance for symmetric supercapacitors, Mater. Design 111 (2016) 44-50.
33. Sun D, Yan X, Lang J, Xue Q. High performance supercapacitor electrode based on graphene paper via flame-induced reduction of graphene oxide paper, J. Power Sources 222 (2013) 52-58.
34. Xu Z, Li Y, Li D, Wang D, Zhao J, Wang Z. et al., N-enriched multilayered porous carbon derived from natural casings for high-performance supercapacitors, Appl. Surf. Sci. 444 (2018) 661-671.
35. Han X, Jiang H, Zhou Y, Hong W, Zhou Y, Gao P. et al., A high performance nitrogen-doped porous activated carbon for supercapacitor derived from pueraria, J. Alloys Compd. 744 (2018) 544-551.
36. Zhang G, Chen Y, Chen Y, Guo H. Activated biomass carbon made from bamboo as electrode material for supercapacitors, Mater. Res. Bull. 102 (2018) 391-398.
37. Ma G, Ran F, Peng H, Sun K, Zhang Z, Yang Q. et al., Nitrogen-doped porous carbon obtained via

one-step carbonizing biowaste soybean curd residue for supercapacitor applications, Rsc Advances 5 (2015) 83129-83138.
38. Han X, Jiang H, Zhou Y, Hong W, Zhou Y, Gao P. et al., A high performance nitrogen-doped porous activated carbon for supercapacitor derived from pueraria, J. Alloys Compd. 744 (2018) 544-551.
39. Zhang X, Niu Q, Guo Y, Gao X, Gao K, Heteroatom-doped porous carbons derived from moxa floss of different storage years for supercapacitors, Rsc Advances. 8 (2018) 16433–16443.
40. Zhang G, Chen Y, Chen Y, Guo H. Activated biomass carbon made from bamboo as electrode material for supercapacitors. Materials Research Bulletin. 2018;102: 391-398.
41. Chen L, Ji T, Mu L, Zhu J. Cotton fabric derived hierarchically porous carbon and nitrogen doping for sustainable capacitor electrode. Carbon. 2017;111: 839-848.
42. Wu Y, Cao J-P, Zhao X-Y, et al. Preparation of porous carbons by hydrothermal carbonization and KOH activation of lignite and their performance for electric double layer capacitor. Electrochimica Acta. 2017;252: 397-407.
43. Dai C, Wan J, Yang J, et al. H_3PO_4 solution hydrothermal carbonization combined with KOH activation to prepare argy wormwood-based porous carbon for high-performance supercapacitors. Applied Surface Science. 2018; 444: 105-117.
44. Thomas E. R, Denisa H-J, Kiran K, Zhonghua Z, Gao Q. L, Microstructure and electrochemical double-layer capacitance of carbon electrodes prepared by zinc chloride activation of sugar cane bagasse. Journal of Power Sources. 2010; 195: 912–918
45. María J. M-L., Diego C. A., Novel designs of carbon electrodes for the technological improvement of electrochemical capacitors. Smart Supercapacitors: Fundamentals, Structures, and Applications, 2023, pages 321-358.
46. Nitrogen (Fixed)--Ammonia (2022)" (PDF). U.S. National Minerals Information Center. Retrieved 24 January 2023.